*Article*

# In Situ Decoration of ZnSnO$_3$ Nanosheets on the Surface of Hollow Zn$_2$SnO$_4$ Octahedrons for Enhanced Solar Energy Application

**Zhengdao Li [1,2,*], Kecheng Liu [1], Ruixue Sun [1], Chuanyun Yang [1,2] and Xiaodi Liu [1,*]**

[1] Chemistry and Pharmaceutical Engineering College, Nanyang Normal University, Nanyang 473061, China; liukecheng2006@126.com (K.L.); ruixuesun@126.com (R.S.); ycy_chemistry@163.com (C.Y.)

[2] Engineering Technology-Research Center of Henan Province for Solar Catalysis, Nanyang Normal University, Nanyang 473061, China

[*] Correspondence: nylzd@nynu.edu.cn (Z.L.); liuxiaodiny@126.com (X.L.); Tel.: +86-377-63-513-735 (Z.L.)

**Abstract:** Hierarchical ZnSnO$_3$/Zn$_2$SnO$_4$ porous hollow octahedrons were constructed using the method of combining the acid etching process with the in situ decoration technique for photovoltaic and photocatalytic applications. The composite was used as photoanode of the dye-sensitized solar cells (DSSCs), an overall 4.31% photovoltaic conversion efficiency was obtained, nearly a 73.1% improvement over the DSSCs that used Zn$_2$SnO$_4$ solid octahedrons. The composite was also determined to be a high-performance photocatalyst for the removal of heavy metal ion Cr (VI) and antibiotic ciprofloxacin (CIP) in single and co-existing systems under simulated sunlight irradiation. It was remarkable that the composite displayed good reusability and stability in a co-existing system, and the simultaneous removal performance could be restored by a simple acid treatment. These improvements of solar energy utilization were ascribed to the synergetic effect of the hierarchical porous hollow morphology, the introduction of ZnSnO$_3$ nanosheets, and the heterojunction formed between ZnSnO$_3$ and Zn$_2$SnO$_4$, which could improve light harvesting capacity, expedite electron transport and charge-separation efficiencies.

**Keywords:** ZnSnO$_3$/Zn$_2$SnO$_4$; hierarchical hollow octahedron; dye-sensitized solar cells; simultaneous removal; photocatalytic activity

## 1. Introduction

Synthesis of ternary metal oxides with controllable sizes and shapes has been an active research field in the past two decades, because of their size- and shape- dependent physical, chemical, optical, electronic, and catalytic properties [1–3]. In particular, the two zinc stannates, Zn$_2$SnO$_4$ and ZnSnO$_3$, have caused considerable attention due to their wide applications in dye-sensitized solar cells (DSSCs) [4,5], gas sensors [6,7], lithium-ion batteries [8,9], and photocatalysts [10,11]. Zn$_2$SnO$_4$ and ZnSnO$_3$ are both photovoltaic and photocatalytic materials with band gaps of about 3.6 eV and 3.2 eV, and the Femi energy level of ZnSnO$_3$ is higher than that of Zn$_2$SnO$_4$ [12,13]. When ZnSnO$_3$ is coupled with Zn$_2$SnO$_4$, the heterojunction would form at the interface between the two ternary metal-oxide semiconductors, and the electrons would transfer from the conduction band of ZnSnO$_3$ to that of Zn$_2$SnO$_4$ until the system reaches equilibrium of Fermi energy level [13]. This process will promote the separation of photogenerated electron–hole pairs and thus increase the performance of the DSSCs and photocatalysts. Therefore, the composite consisting of Zn$_2$SnO$_4$ and ZnSnO$_3$ has been successfully synthesized to improve device performance [13]. For example, the ZnSnO$_3$/Zn$_2$SnO$_4$ acted as photocatalyst for degradation of Intracron Blue, and achieved high performance under UV illumination due to lower recombination of electron-hole pairs [14]. The mixed phases of ZnSnO$_3$ and Zn$_2$SnO$_4$ were

used as photoanodes in DSSCs, and it was found the ferroelectric polarization would aid in obtaining relatively high fill factors and open-circuit voltage values in the devices [15].

The published research studies have demonstrated that the three-dimensional hierarchical architectures assembled from the one- or two- dimensional nanostructured building blocks are an interesting class of materials with an abundant variety of tunable physicochemical properties [16]. Hierarchical porous hollow microstructures composed of single-crystalline two-dimensional nanosheets can provide low material density, good surface permeability, high surface area and electron transport rate, as well as high light-harvesting efficiency for application areas of catalysis and photovoltaic devices [17,18]. In this structure system, the material with micrometer-sized diameters can act as light scattering centers to increase the light harvesting of the photoanodes and photocatalysts, which is one of the crucial factors of improving the photovoltaic conversion efficiency of DSSCs and photocatalytic activity [19]. The multiple-reflection inside hollow interior can provide more opportunities for the photoanodes and photocatalysts to trap the incident light for an enhanced light utilization [20,21]. The porous hollow structures possess a large surface area, and to a great extent enhance the mass transportation and the diffusion of liquid reactant in the active layers, meanwhile, the high porosity can provide rich channels with the sizes from nanometer to micron for the surface accessibility [22]. In addition, nanosheets can offer direct pathways for photogenerated electrons, which will result in enhanced electron transport rates [23]. Hence, the hierarchical porous hollow semiconductors were acknowledged as the ideal candidates for the high-performance DSSCs and photocatalysts. However, as far as we know now, there was scarcely any previous research on hierarchical porous hollow $ZnSnO_3/Zn_2SnO_4$ with the view of the photovoltaic and photocatalysis fields simultaneously.

In our recent work, well-defined octahedral $Zn_2SnO_4$ was synthesized through a chemical solution route, and these $Zn_2SnO_4$ micro-crystals were converted to hollow octahedrons by an acid etching process. Whereafter, by means of an in situ growth method, $ZnSnO_3$ nanosheets were intentionally introduced on the surface of hollow $Zn_2SnO_4$ octahedrons to construct the hierarchical porous hollow $ZnSnO_3/Zn_2SnO_4$ octahedrons [12] (Scheme 1). In this paper, the as-prepared hollow $ZnSnO_3/Zn_2SnO_4$ octahedrons were used as photoanodes of DSSCs to evaluate their photovoltaic performance. Meanwhile, the photocatalytic properties of the composite under simulated sunlight irradiation were evaluated by the removal of antibiotic ciprofloxacin (CIP) and heavy metal ion Cr(VI) in single and co-existing systems. Significantly, the $ZnSnO_3/Zn_2SnO_4$ composite consisting of the two ternary metal oxides presented distinct advantages and had a higher photovoltaic conversion efficiency and better removal performance than solid and hollow $Zn_2SnO_4$ octahedrons. In addition, the morphology, crystal structure, optical properties and photocatalytic stability of the composite were investigated via various characterization methods, and the causes of enhanced photovoltaic and photocatalytic performance were proposed and discussed in detail.
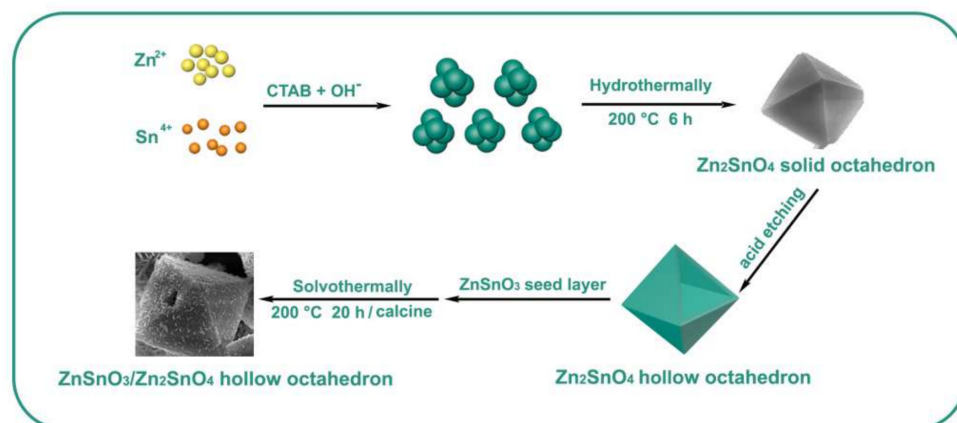


**Scheme 1.** Schematic illustration for the formation of the three samples.

## 2. Materials and Methods

### 2.1. Materials Synthesis

All chemicals were purchased from Shanghai Aladdin Bio-Chem Technology Co. Ltd. (Shanghai, China) and used without purification. $Zn_2SnO_4$ solid octahedron ($S_1$), $Zn_2SnO_4$ hollow octahedron ($S_2$), hierarchical $ZnSnO_3/Zn_2SnO_4$ hollow octahedron ($S_3$), and $ZnSnO_3$ nanosheets were prepared according to a reported procedure in our previous paper [12], and more details are described in the "Materials Synthesis" section in the Supplementary Materials.

### 2.2. Materials Characterization

The scanning electron microscopy (SEM, FEI NOVA NanoSEM230) and transmission electron microscopy (TEM, JEOL 3010) images were collected to obtain the morphology information of the samples. The compositions were analyzed by X-ray diffraction (XRD) (Rigaku, Tokyo, Japan) with Cu Ka radiation ($\lambda = 1.54056$ Å).

### 2.3. Preparation of the Electrode

An amount of 1 g of as-prepared sample powder and a certain amount of absolute ethanol were put into a mortar and stirred for 30 min. An amount of 4 g of the ethanol solution of two ethyl celluloses and 2 g of anhydrous terpineol were added, and the homogenization was performed using a sonicator (Vibra cell 72408, Bioblock Scientific, Wasserbad, Germany). The contents were concentrated by evaporator with 120 mbar at 38 °C and the pastes were finalized. Fluorine-doped tin oxide (FTO) conductive glass was cleaned with dilute acid and alkali solution, ethanol and deionized water several times in the ultrasonic cleaner. A doctor-blade technique was employed to coat paste onto the surface of FTO. The film was dried at 125 °C, annealed at 450 °C for 30 min and sintered at 500 °C for 15 min in the air to form the working electrodes. Typically, to improve the connection among $ZnSnO_3/Zn_2SnO_4$ hollow octahedrons, the as-prepared working electrodes were immersed into $ZnSnO_3$ sol for 30 min, then sintered at 500 °C for another 30 min.

A magnetron sputter platinum mirror acted as the counter electrode. Dye sensitization was accomplished by immersing a film in 0.3 mM dye solution (solvent mixture of tert-butyl alcohol and acetonitrile in a volume ratio of 1:1) at 80 °C over *a set length of time*. Here, the dye used in the DSSCs was cis-bis (isothiocyanato) bis (2,2′-bipyridyl-4,4′-dicarboxylato) ruthenium-(II) bis-tetrabutylammonium (also known as N719) [24]. The electrolyte contained 0.5 M tert-butylpyridine, 0.5 M LiI and 0.05M $I_2$ in acetonitrile. The FTO substrate, film, and counter electrode constituted a sandwich-like cell structure (Figure S1).

### 2.4. Photovoltaic Characterization

Electrochemical impedance spectroscopic (EIS) measurements were carried out with a PAR2273 workstation (Princeton Applied Research, Oak Ridge, TN, USA). The current–voltage (J-V) characteristics were measured with an active area of 0.16 $cm^2$ on an Oriel 92251A-1000 on a Keithley 236 source measurement unit. An Oriel 92251A-1000 sunlight simulator was used as the light source (AM1.5, 100 mW $cm^{-y}$). Intensity-modulated photocurrent/photovoltage spectra (IMPS/IMVS) were recorded on an electrochemical workstation (Zahner, Zennium, Kansas City, MO, USA). The incident photon-to-current efficiency (IPCE) was investigated on a PEC-S20 instrument (Peccell, Yokohama-shi, Japan). The film thickness was measured by a computerized profilometer (Dektak 3, Ulvac, Chigasaki, Japan). The dye-loading amount of photoanodes was ascertained by desorbing the dye into 10 mL of 0.1 M NaOH water solution and quantified by measuring N719 optical adsorption peak intensity.

### 2.5. Photocatalytic Measurements

The photocatalytic activities of the different photocatalysts were evaluated by the removal of CIP and Cr(VI) using a 500 W xenon lamp as an irradiation source. Photocata-

lyst (75 mg) was added into 150 mL of CIP (10 mg/L) or/and $K_2Cr_2O_7$ (50 mg/L) single contaminant or contaminant mixture. To achieve adsorption-desorption equilibrium, the suspension was continuously stirred for 24 h at room temperature in the dark. During the catalytic reaction, at the given intervals, 5 mL of suspension was collected and centrifuged with $4000\times$ *g* rpm for 5 min to remove the photocatalyst. The concentration of Cr(VI) was estimated using the standard diphenylcarbazide analytical method at 540 nm with a UV-Vis spectrometer. The contents of CIP were analyzed by detecting the values of feature absorbance of 277 nm on a UV–Vis spectrometer. To study the reusable ability of the photocatalysts, the used samples were collected and washed with deionized water to remove the residual materials, followed by drying at 60 °C, and then the cycling experiments were conducted at optimal operating conditions.

## 3. Results and Discussion

### 3.1. Structure Characterization

The SEM image in the Figure S2a clearly demonstrated that the typical $S_1$ showed the octahedral morphology with an average size of ~1.2 μm and possessed smooth surfaces. After a simple acid etching process, these $Zn_2SnO_4$ octahedrons still maintained their original size and shape whilst also having rough surfaces (Figure S2b). As with design, $S_1$ converted into hollow structure, which could be confirmed by the TEM image of Figure S2c, to gain the sample $S_2$. As can be seen from the Figure S2d, the $ZnSnO_3/Zn_2SnO_4$ composite remained octahedron-like in structure, and the nanosheets of ~50 nm length and ~15 nm thickness distributed on each facet of the octahedron to form a hierarchical structure. Additionally, the TEM image revealed that the hollow structure was not damaged through the solvothermal process of $ZnSnO_3$ nanosheet growth (Figure S2e).

Figure S3 presented the XRD spectra of the three samples. All the diffraction peaks of $S_1$ and $S_2$ could be assigned to the cubic phase $Zn_2SnO_4$ (JCPDS: 24-1470), this result illustrated that no change of composition and crystal form transformation emerged during the acid etching process. For the cases of $S_3$, the additional XRD peaks characteristic of $ZnSnO_3$ (JCPDS No. 28-1486) confirmed that $S_3$ was $ZnSnO_3/Zn_2SnO_4$ composites.

To construct an energy band diagram for $S_1$, $S_2$ and $S_3$, the band gap energies ($E_g$) and flat-band potentials ($E_{fb}$) of the three samples should be determined. As shown in Figure 1a, the wavelength threshold of the pristine solid and hollow $Zn_2SnO_4$ octahedrons located at 340 nm and 360 nm, separately, and $ZnSnO_3/Zn_2SnO_4$ hollow octahedrons displayed the red-shifted light absorption in comparison with pure $Zn_2SnO_4$, which was helpful to extend the light absorption. The $E_g$ was estimated according to the Kubelka-Munk function equation to be around 3.83 eV for $S_1$, 3.59 eV for $S_2$ and 3.43 eV for $S_3$ (the inset of Figure 1a). The positive slopes for Mott–Schottky plots indicated the characteristics of n-type semiconductors for the three samples, and the $E_{fb}$ values were calculated to be $-1.15$, $-1.15$ and $-1.29$ V for $S_1$, $S_2$ and $S_3$ (vs. Ag/AgCl, pH = 7), respectively, from the tangential intercept of the curves (Figure 1b). Then, the conduction band (CB) potentials of $S_1$, $S_2$ and $S_3$ could be determined to be $-0.93$, $-0.93$ and $-1.07$ V (vs NHE, pH = 7), respectively, from the formula (Equation (1)) [25]:

$$E_{NHE} = E_{Ag/AgCl} - E^\theta + 0.059 \text{ pH} \tag{1}$$

where $E^\theta$ and $E_{Ag/AgCl}$ represent standard electrode potentials and the Ag/AgCl electrode potential at pH = 7 (0.197 V), respectively. According to the formula ($E_{VB} = E_{CB} + E_g$), the valence band (VB) potentials of $S_1$, $S_2$ and $S_3$ were calculated to be 2.90, 2.66 and 2.36 V, respectively. Based on the $E_{fb}$, $E_{CB}$ and $E_{VB}$ values of the three samples (Table S1), their energy band constructions were depicted in Scheme 2a. For the three materials, the bottom of CB and the top of VB were lower than lowest unoccupied molecular orbital (LUMO, $-1.5$ eV vs. NHE) and the highest occupied molecular orbital (HOMO, +1.1 eV vs. NHE) energy levels of N719 dye, respectively, and match well with the redox couple in the electrolyte, ensuring the operation of the DSSCs [26].
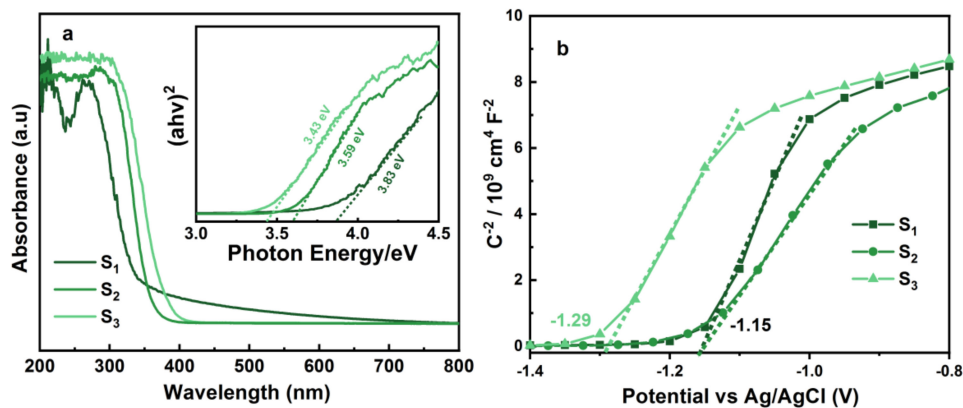
**Figure 1.** (**a**) UV−_vis absorption spectra; (**b**) Mott−Schottky plots of the samples; Inset of (**a**): the corresponding Tauc's curves.
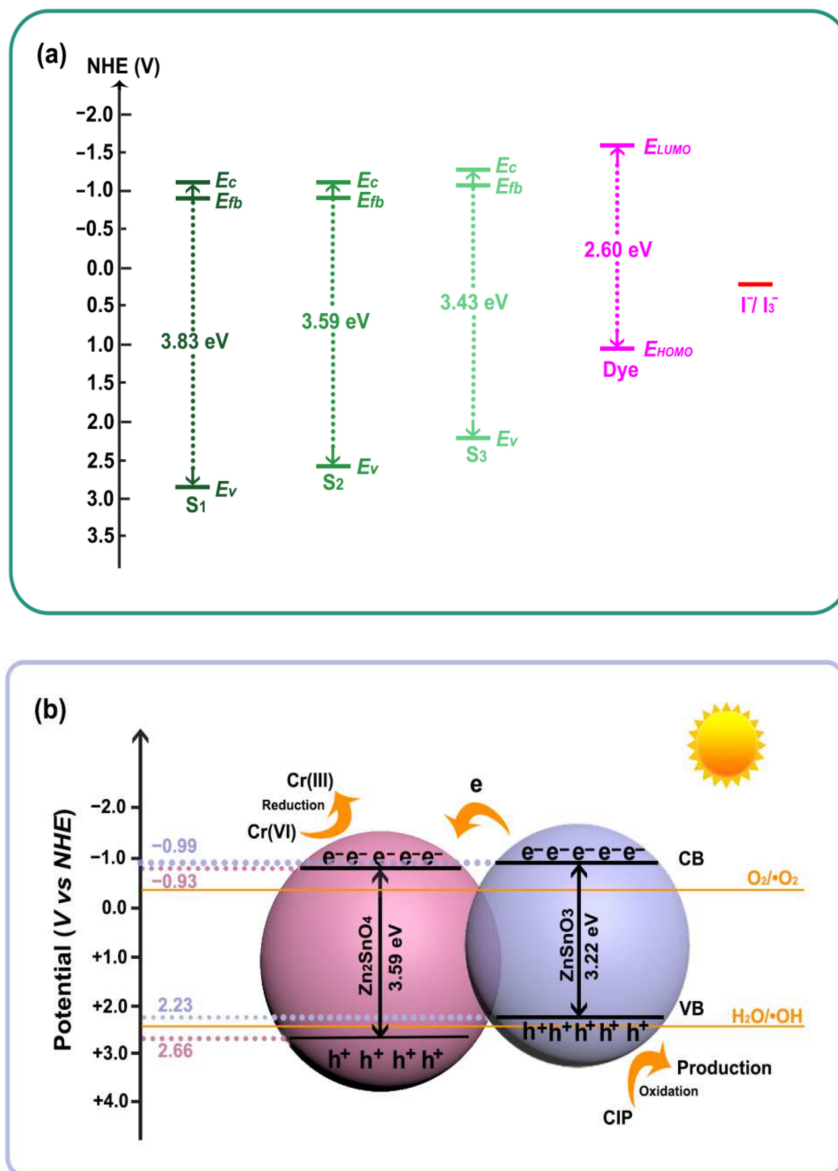


**Scheme 2.** (**a**) Energy band construction of three samples; (**b**) Schematic diagram of the band structure and charge separation in $ZnSnO_3/Zn_2SnO_4$ composite.

*3.2. Photovoltaic Characteristics of $Zn_2SnO_4$ and $ZnSnO_3/Zn_2SnO_4$*

3.2.1. Photovoltaic Characteristics of $Zn_2SnO_4$

Four DSSCs based on the $Zn_2SnO_4$ solid octahedrons photoanodes with the same thickness of ~10 μm were sensitized with various sensitization durations to examine the optimum immersion time in N719 dye solution (Table S2). Under 1 sun AM 1.5 illumination, the short-circuit current ($J_{sc}$) increased with the sensitization time in the initial 6 h, while the open-circuit voltage ($V_{oc}$) and fill factors (FF) remained stable, then the photovoltaic conversion efficiency ($\eta$) reached the maximum 2.35% at 6 h. However, a decrease in the FF, $J_{sc}$ and $\eta$ were observed at 8 h later probably because of the formation of aggregates, as in the case of $Zn_2SnO_4$ [27]. Reduced $V_{oc}$ was largely due to the formation of $Zn^{2+}$/dye complex. The immersion time was longer, a complex layer could be observed and formed a thick covering layer, which was therefore inactive for electron injection [28]. These results suggested that the optimal sensitization time was six hours in the acidic dye molecules. To explore the effect of film thickness on $\eta$ of DSSCs, solid $Zn_2SnO_4$ films with the different thicknesses of 6, 9, 12, 15 and 18 μm were prepared and the detailed photovoltaic parameters of DSSCs based on these photoelectrodes are summarized in Table S3. In effect, when the thickness varied from 6 μm to 12 μm, the thicker film could adsorb much more dye to enhance the light harvesting ability of the photoanode, and then $J_{sc}$ significantly increased from 4.17 to 5.65 mA cm$^{-2}$. As the film thickness increased continuously to 15 μm or thicker, the more trapping sites and electron recombination centers would generate, so the more serious electron recombination would lower the electrons concentration, and hence lead to the decline of $J_{sc}$, $\eta$ [29] and $V_{oc}$ [30]. For the optimized DSSCs based on $Zn_2SnO_4$ solid octahedrons, the $\eta$, $V_{oc}$, $J_{sc}$ and FF were 2.49%, 0.64 V, 5.65 mA cm$^{-2}$ and 68.79%, respectively.

To study the effect of the hollow structure on the photovoltaic properties of DSSCs, $Zn_2SnO_4$ hollow octahedron photoelectrodes were prepared by depositing 12 μm film on FTO glass, and photovoltaic properties were tested by constructing DSSCs. The characteristic *J*-V curves and their photovoltaic parameters are given in Figure 2a. It can be seen that the $V_{oc}$ and FF of $S_2$-based DSSCs were similar to those of $S_1$-based DSSCs, the distinct photovoltaic behavior of $S_2$ was larger $J_{sc}$ (7.61 mA cm$^{-2}$) compared to $S_1$ (5.65 mA cm$^{-2}$). The relatively high $J_{sc}$ of $S_2$ can be considered following the three combined effects: (1) Higher dye loading, due to larger specific surface area. The measured dye-loading amount for the $S_2$ film was around $4.23 \times 10^{-7}$ mol·cm$^{-2}$ μm$^{-1}$, and was more than that of the $S_1$ film ($2.87 \times 10^{-7}$ mol·cm$^{-2}$ μm$^{-1}$). The surface area of $S_2$ was measured as 37.7 m$^2$ g$^{-1}$ (Figure S4), 70.6% higher than that of $S_1$ (22.1 m$^2$ g$^{-1}$). So, the larger specific surface area enabled $S_2$ to adsorb more dye to improve $J_{sc}$ of DSSCs. (2) Stronger light-harvesting efficiency, due to the hollow structure. The corresponding UV–vis absorption spectra of solid and hollow $Zn_2SnO_4$ octahedrons displayed a strong absorption peak in the ultraviolet region, and the absorption intensity of the latter was stronger than that of the former (Figure 1a). Because of the same crystal structure, the enhanced light absorption of $S_2$ was presumably due to its hollow structure, as explained in Figure S5. Obviously, in case of $Zn_2SnO_4$ hollow octahedrons, the empty internal structure could offer more interfaces to considerably increase the chance of light reflections, leading to the more efficient utilization of the incident light and increased light-harvesting efficiency, and then more photogenerated electron-hole pairs would generate when $S_2$ was under light irradiation [31,32]. (3) Efficient electrolyte diffusion into the interior of the hollow octahedrons, due to mesoporous wall. The results of $N_2$ adsorption/desorption confirmed the existence of the mesoporous microstructure for $Zn_2SnO_4$ hollow octahedrons (Figure S4). The pore-size distribution indicated that the average pore size for $S_2$ was about 3.6 nm, which would promote electrolytes to transport in the photoelectrode and enter the internal area of hollow octahedrons to increase the contact probability between electrolyte and electrodes to improve the $\eta$ of DSSCs.
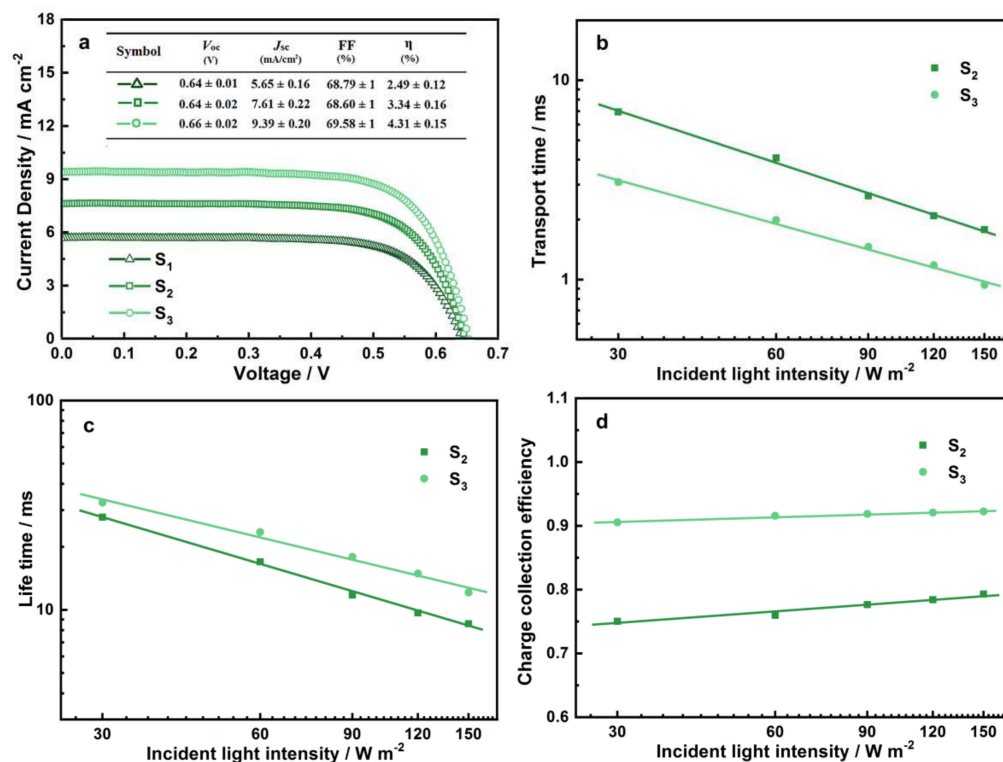
**Figure 2.** (**a**) $J-V$ curves for the DSSCs based on the different electrodes; (**b**) Transport time, (**c**) Lifetime and (**d**) the charge collection efficiency of the different DSSCs.

### 3.2.2. Photovoltaic Characteristics of $ZnSnO_3/Zn_2SnO_4$

To investigate the influence of the $ZnSnO_3$ nanosheets on the electron transfer and recombination behaviors, the IMPS/IMVS measurements of $S_2$ and $S_3$ were performed. The IMPS/IMVS measurements could provide direct evidence of the electron transport time ($\tau_t$) and electron recombination time ($\tau_r$) through the equations [33]:

$$\tau_t = 1/(2\pi f_t) \tag{2}$$

$$\tau_r = 1/(2\pi f_r) \tag{3}$$

where $f_t$ ($f_r$) is the minimum frequency of the IMPS(IMVS) imaginary component. Here, $\tau_t$ and $\tau_r$ characterize the electron transport properties in photoanode films and recombination with redox species in the electrolyte, respectively. Hence, smaller $\tau_t$ and larger $\tau_r$ mean a faster transport rate and slower recombination rate. Examinations of Figure 2b,c clearly showed that the $\tau_t$ ($\tau_r$) of the DSSCs based on $S_3$ photoanodes was shorter (longer) than that of $S_2$ over light intensities from 30 to 150 W m$^{-2}$. This finding was a consequence of the following reasons: first, the engineered interfacial design of band-structure-matched $ZnSnO_3/Zn_2SnO_4$ composite photoanodes. A schematic illustration of the energy levels of $ZnSnO_3$ and $Zn_2SnO_4$ is shown in Scheme 2b, the CB edge of $ZnSnO_3$ was determined to be $-0.99$ V (Figure S6), which was more negative than that of $Zn_2SnO_4$ ($-0.93$ V, Table S1), such an energy band matching composite photoanode would serve as the "bridge" to expedite electron transport from excited $ZnSnO_3$ to FTO resulting in shorter $\tau_t$ [34]. The band-structure-matched $ZnSnO_3/Zn_2SnO_4$ photoanodes, meanwhile, to some extent avoid any extra internal traps, and could effectively suppress the recombination between the electron in the CB of composite photoanodes and $I_3^-$ in the electrolyte, which rationalizes the reasons for the increase in $\tau_r$. Second, the two-dimensional $ZnSnO_3$ nanosheets in the composite photoanodes caused direct electron transport paths and were beneficial for faster electron transport. Besides, it is well known that the less trap sites there are, the slower charge recombination occurs [35]. Compared to the nanoparticles with abundant

grain boundaries, ZnSnO3 nanosheets exhibited a reduced recombination loss, which can contribute to longer $\tau_r$. Third, interconnected contact between the $ZnSnO_3$ nanosheets of neighboring octahedrons made the contact area larger and prolonged the electron transport channel of the injected electrons, so lead to fast electron transport to the back contact, thus a lower recombination rate [36]. These results verified the reasonableness of the promoting the electron transfer of the $ZnSnO_3$ nanosheets in the composite film.

To evaluate the scattering effect of the $ZnSnO_3$ nanosheets, the diffuse reflection spectra of the films made from $S_2$ and $S_3$ were measured (Figure 3a). Compared to the $Zn_2SnO_4$ film, the composite film had higher diffuse reflection ability in the wavelength region from 380 to 800 nm, suggesting that the vertical $ZnSnO_3$ nanosheets would lead to more significant incident light scatter within the composite films. A possible explanation can be that $S_3$, owing to the surface $ZnSnO_3$ nanosheets, can scatter the incident light to all directions, as schematically illustrated in Scheme 3. Thereby, the composite film utilized the incident light to a higher degree than that in the case of $S_2$. At the same time, this scattering capacity could provide more chances for the N719 molecules on the composite area to trap photons, and then turn into electrons [26]. Otherwise, compared with $S_2$, the absorption edge (~390 nm) of $S_3$ exhibited red shift (Figure 1a), implying more holes and electrons can be generated after $ZnSnO_3$ incorporation, which probably was attributed to the interaction between $ZnSnO_3$ and $Zn_2SnO_4$. These results confirmed the positive impact of the $ZnSnO_3$ nanosheets in the composite film on the light harvesting efficiency.
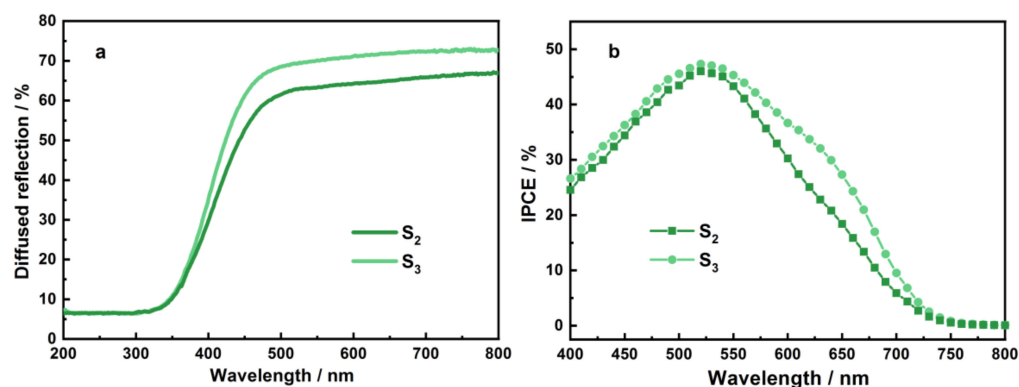


**Figure 3.** (**a**) Diffuse reflectance spectra and (**b**) IPCE spectra of the different electrodes.
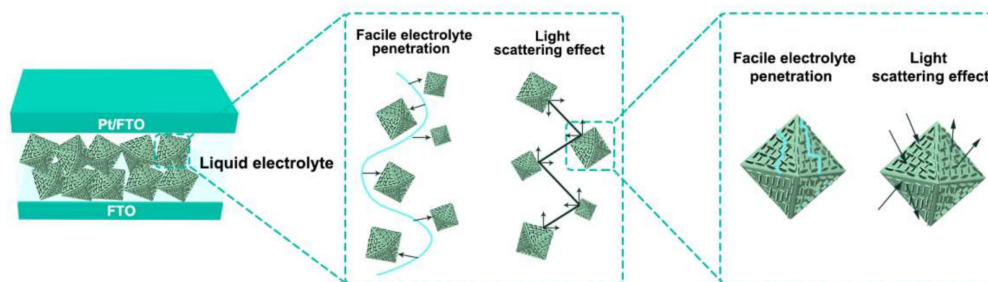


**Scheme 3.** Schematic representation of (**left**) a DSSC with $ZnSnO_3/Zn_2SnO_4$ hollow octahedron film, (**center**) facile penetration of electrolyte through the hollow octahedrons and light scattering effect by the octahedrons, and (**right**) a single octahedron showing penetration of an electrolyte through it.

To evaluate the beneficial impact of the addition of the $ZnSnO_3$ nanosheets on the photovoltaic conversion properties, the composite was applied as photoanodes of DSSCs. Four $ZnSnO_3/Zn_2SnO_4$ DSSCs with the same thickness (~12 μm) were fabricated with various sensitization durations. The $\eta$ gradually increased with the sensitization time and reached the maximum at 4 h (Table S4). Figure 2a shows the *J–V* curves of the DSSCs based on the optimized composite photoanode film DSSCs. Compared with DSSCs based on $S_2$, the addition of $ZnSnO_3$ nanosheets to $Zn_2SnO_4$ cells resulted in considerable improvement

in $V_{oc}$, $J_{sc}$ and FF, so the DSSCs with $S_3$ exhibited an enhanced $\eta$ (4.31%) value by around 27.9% as compared with $S_2$ DSSCs (3.34%). It can be seen that the $V_{oc}$ of the $S_3$ (0.66 V) was higher than that obtained from the $S_2$ (0.64 V). The $V_{oc}$ is determined by the chemical potential of the electrolyte and the Fermi level of the semiconductor oxide [37]. As seen in Scheme 2a, the $S_3$ showed a more negative $E_{fb}$ value, so the difference between the Fermi level of $S_3$ and the redox potential of $I^-/I_3^-$ would be larger, and the corresponding $V_{oc}$ will be higher. On the other hand, through the analysis of the IMVS and IMPS dates above, the introduction of $ZnSnO_3$ nanosheets in the $Zn_2SnO_4$ film can inhibit electron recombination and prolong electron lifetime, which could increase the $V_{oc}$. So, the enhanced $V_{oc}$ with $ZnSnO_3$ nanosheets added should offer the combined impact of the elevated CB edge and the suppressed interfacial charge recombination.

The $J_{sc}$ can be estimated using the following formula [38]:

$$J_{sc} = qI_0\eta_{lh}\eta_{inj}\eta_{cc} \tag{4}$$

where $q$ and $I_0$ are the elementary charge and light flux. Hence, the $J_{sc}$ is directly proportional to the light harvesting efficiency ($\eta_{lh}$), electron injection efficiency ($\eta_{inj}$) and electron collection efficiency ($\eta_{cc}$) of DSSCs. First, the $\eta_{lh}$ is determined by both the dye loading amount and/or the light scattering capability [39]. The absorption quantity of N719 on $S_3$ with the surface area of 41.3 $m^{-2}$ $g^{-1}$ ($4.49 \times 10^{-7}$ mol·cm$^{-2}$ μm$^{-1}$) was slightly larger than that of $S_2$ ($4.23 \times 10^{-7}$ mol·cm$^{-2}$ μm$^{-1}$). Meanwhile, as discussed above, the addition of the $ZnSnO_3$ nanosheets favored enhanced light-harvesting efficiency and originated from light scattering and the red shift of the absorption edge. To further obtain the detailed information on the light harvest of the DSSCs, the IPCE measurements were performed, as shown in Figure 3b. The IPCE value of the $S_3$-cell was higher than that of the $S_2$-cell in whole wavelength range from 400 to 800 nm, indicating that the quantum efficiency of the $S_3$-cell was greater than that of the $S_2$-cell in the visible-light wavelength region [40]. The higher IPCE values for the $S_3$-cell at short wavelengths reflected on its stronger dye-loading capacity. In the longer wavelength region from 600 to 750 nm, the increased IPCE values of the $S_3$-cell could be explained by the enhanced light scattering efficiency, which promotes the light harvesting of the N719 dye in this region. Further, the IPCE measurements also validated the estimated $J_{sc}$ values (Figure S7) and correlated well with those obtained from the J-V curves (Figure 2a). Those studies indicated superior light harvesting efficiency of $S_3$ films compared to $S_2$ films. Second, $\varphi_{inj}$ is the probability of electron injection from the dye-excited state into the CB of the semiconductor. The CB was moving upward in the $S_3$ film, which meant that charge injection from LUMO of N719 dye to the CB of $S_3$ would be limited, thus reducing $\varphi_{inj}$. Third, the $\eta_{cc}$ can be estimated according to $\tau_t$ and $\tau_r$ [33].

$$\eta_{cc} = 1 - \tau_t/\tau_r \tag{5}$$

Figure 2d showed the $\eta_{cc}$ of the $S_3$-cell was superior to the $S_2$-cell under various light intensities, which is attributed to the incorporation of $ZnSnO_3$ nanosheets enhancing the electron transfer. In summary, although the $\varphi_{inj}$ values would proportionally decrease, the $S_3$ showed an increased $J_{sc}$ because the $\eta_{lh}$ and $\eta_{cc}$ were raised more significantly than the decrease in $\varphi_{inj}$.

A comparison of photovoltaic performances between our assembled DSSCs and previously reported DSSCs is summarized in Table S5, including $J_{sc}$, $V_{oc}$, FF and $\eta$. It can be seen that, the $\eta$ of the DSSC based on $ZnSnO_3/Zn_2SnO_4$ hollow octahedrons was not higher than that of $Ba^{2+}$ ion doped $Zn_2SnO_4$ nanocrystalline [41], the cause was probably that the photo sensitizer was a mixture including N719 dye and D131 dye instead of only N719. The DSSC based on $ZnSnO_3/Zn_2SnO_4$ hollow octahedrons showed superior photovoltaic performances compared to metallic silver decorated $Zn_2SnO_4$ spheres [42], Au inlaid $Zn_2SnO_4/SnO_2$ hollow rounded cubes [43], the binary metal oxide MgO passivation layers modified $Zn_2SnO_4$ nanoparticles [44], and $ZnO/Zn_2SnO_4$ core shell photoanodes [45]. In

addition, the higher FF showed the advantage of $ZnSnO_3/Zn_2SnO_4$ hollow octahedrons in practical application [46].

### 3.3. Photocatalytic Performance

In order to further demonstrate the beneficial effect of the $ZnSnO_3$ nanosheets on photocatalytic activity, $S_2$ and $S_3$ were used to perform photocatalytic removal of CIP and Cr(VI) in single and co-existing systems under simulated sunlight. A blank control experiment was carried out to confirm that CIP would hardly self-degrade under the condition of no photocatalyst (Figure 4a). Initially, only 64.3% of CIP was degraded by $S_2$ within 105 min of light irradiation. With the addition of $ZnSnO_3$, the catalyzed degradation efficiency of the composites reached 94.3% within same irradiation time length. As shown in Figure 4b, the photodegradation of CIP catalyzed by $S_2$ and $S_3$ followed a pseudo-first-order rate law (Table S6), $\ln (C_0/C_t) = kt$, where $k$ is the degradation rate constant, $C_0$ and $C_t$ are the concentrations of the pollutant solution before light irradiation and at irradiation time $t$, respectively. The $k$ values of $S_2$ and $S_3$ were 0.010 and 0.026 min$^{-1}$ (Figure 4b), respectively, and the photodegradation rate constant of $S_3$ was around 2.6 times higher than that of $S_2$. The solution of Cr(VI) was also treated to investigate the photoreduction performance of photocatalyst. As shown in Figure 4c, the reduction of Cr(VI) was almost negligible in the absence of the photocatalyst, and the Cr(VI) concentration was decreased by the processes of simulated sunlight. In 200 min, 60.5% and 87.1% photoreduction efficiency was observed using $S_2$ and $S_3$, respectively. The kinetic constant 0.010 min$^{-1}$ of $S_3$ was numerically about 2.50 times as high as $S_2$ at 0.004 min$^{-1}$ (Figure 4d). All these showed, compared with the $S_2$ sample, that the $S_3$ photocatalyst displayed stronger removal efficiency under illumination, which verified that the addition of $ZnSnO_3$ nanosheets effectively enhanced system photocatalytic performance. For further research, the simultaneous photocatalytic CIP oxidation and Cr(VI) reduction over $S_3$ were performed in the co-existing systems containing CIP (10 mg/L)/$K_2Cr_2O_7$ (50 mg/L). $S_3$ only removed a small amount of CIP and Cr(VI) under a no-light condition, which showed no simulated sunlight response (Figure 5a). Compared with the photodegradation results in Figures 4 and 5b, the higher CIP removal performance presented after the introduction of Cr(VI) in the system, and the $k$ value increased from 0.026 min$^{-1}$ without Cr(VI) to 0.033 min$^{-1}$ with co-existence of Cr(VI). Meanwhile, the removal rate of Cr(VI) increased with co-existence of CIP, and the k value of $S_3$ in the mixed solution was 1.70 times as high as in the absence of CIP. The results of the experiment suggested the synergistic effect between photocatalytic CIP oxidation and Cr(VI) reduction.

The quenching experiments were conducted to further explore the removal mechanism of Cr(VI) and CIP over $S_3$ (Figure S8). In general, ammonium oxalate (AO), isopropyl alcohol (IPA), dimethyl sulfoxide (DMSO) and benzoquinone (BQ) were used to quench the active species photogenerated holes ($h^+$), hydroxyl radicals (OH), photogenerated electrons ($e^-$) and superoxide radicals ($O_2^-$), respectively [47]. It could be observed that the photodegradation efficiencies of CIP decreased evidently with the addition of AO and BQ to the co-existing system, reflecting that $h^+$ and $O_2^-$ had a significant effect in the removal reaction of CIP over $S_3$. In contrast, when the IPA was introduced into this system, there was only a negligible suppression, indicating the influence of ·OH could be ignored. Therefore, $h^+$ and $O_2^-$ were the predominant reactive species in the CIP photocatalytic degradation process. Meanwhile, the photoreduction efficiencies of Cr(VI) obviously decreased from 92.9 to 47.6% with the addition of DMSO, it could be deduced that Cr(VI) was reduced by $e^-$ and the photogenerated electrons served as the main reaction species of the photocatalytic reduction of Cr(VI).

Based on the above results and discussion, a photocatalytic mechanism was proposed (Scheme 2b). When the light irradiated on the photocatalyst, the $ZnSnO_3/Zn_2SnO_4$ composite could be excited by the photon, and equivalent energy would generate the electron-hole pairs. The conduction band of $ZnSnO_3$ ($-0.99$ V) was more negative than that of the hollow $Zn_2SnO_4$ ($-0.93$ V), the photogenerated electrons would easily inject from the former into

the latter through the heterostructure between $ZnSnO_3$ and $Zn_2SnO_4$. Therefore, the photo-generated electron-hole pairs were spatially separated by this heterostructure to restrain the recombination of charges. Cr(VI) was a strong oxidant and could serve as an electron acceptor to consume these generated electrons. Because the $E_{CB}$ of $Zn_2SnO_4$ was more negative than the $O_2/\cdot O_2^-$ potential ($-0.33$ eV) [48], and the electrons would react with the dissolved $O_2$ to produce $O_2^-$. Meanwhile, the valence band of $Zn_2SnO_4$ (2.66 V) was more positive than that of $ZnSnO_3$ (2.23 V), and the holes would migrate simultaneously from VB of $Zn_2SnO_4$ to $ZnSnO_3$ in the opposite direction, whereas, $h^+$ at VB of $ZnSnO_3$ was not more positive than the $H_2O/\cdot OH$ (2.40 eV) [48], and not enough to oxidize $H_2O$ to $\cdot OH$. Hence, the $O_2^-$ and $h^+$ acted as the main oxidants to decompose CIP into small molecules. So, in this co-existing system, the faster photoreduction rate of Cr(VI) and photodegradation efficiency of CIP might be due to the synchronized actions of the CIP as an electron donor and Cr(VI) as an electron acceptor. The oxidation process of CIP and the reduction process of Cr(VI) consumed the photo-excited holes and electrons, respectively. These two processes effectively promoted the separation of photogenerated electrons and holes, and resulted in much more electrons for Cr(VI) reduction and holes for CIP oxidation, and the recombination of photogenerated carriers would be prohibited so as to enhance the photocatalytic efficiency [47].
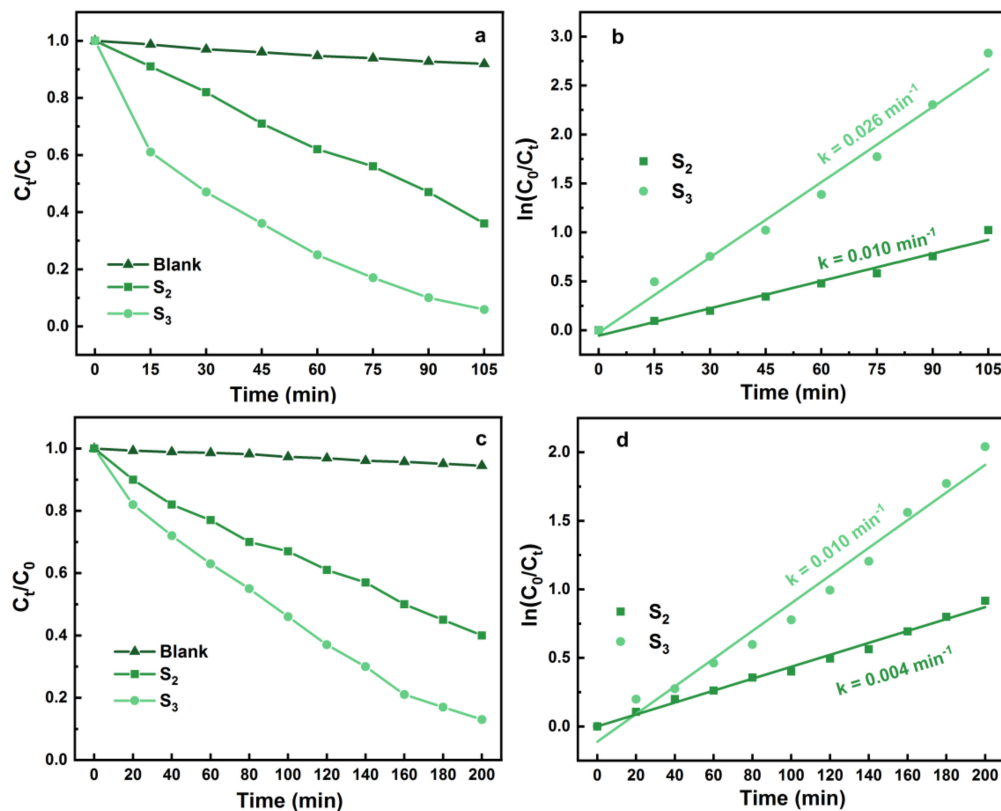


**Figure 4.** Removal efficiency of (**a**) CIP and (**c**) Cr(VI); the first−order kinetics of (**b**) CIP and (**d**) Cr(VI) by different photocatalysts in single system.
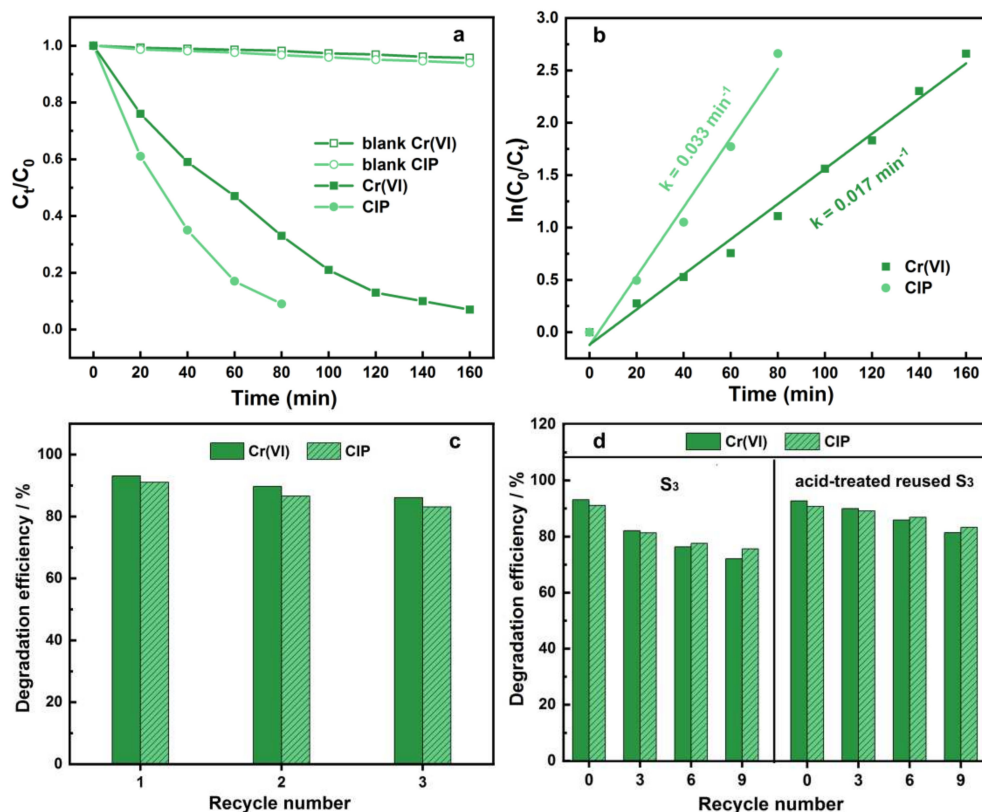
**Figure 5.** (**a**) Removal efficiency of CIP and Cr(VI) in the mixed solutions by $S_3$ sample; (**b**) the corresponding first-order kinetics and rate constants; (**c**) reusable degradation activity of $S_3$ for three cycles; (**d**) simultaneous removal of CIP and Cr(VI) in the presence of $S_3$ with and without acid treatment for nine cycles.

To evaluate the reusable ability of $S_3$ in the co-existing systems, the recycling experiment was conducted under the same conditions. As shown in Figure 5c, after the three cycles of operation, the removal efficiencies changed from 92.7% to 86.1% for Cr(VI) and 91.1 to 83.2% for CIP, and the photocatalytic performance showed less than 9% loss, which confirmed that the $ZnSnO_3/Zn_2SnO_4$ composite possessed outstanding reusability. To further investigate the repeatable removal performance, the number of repeated uses was increased from three to nine, and the photocatalytic efficiency decreased to 71.8% for Cr(VI) and 75.3% for CIP. Borrowed from the previous method [49], after three consecutive cycles, $S_3$ was cleaned with 0.1 mM HCl once to remove the adsorbed pollutant molecules, it was found that $S_3$ with the acid-treatment preserved 88.5 and 89.2% of the initial efficiency for Cr(VI) and CIP in the ninth cycle, and greater than 15.6 and 10.4% photocatalytic efficiency without the acid-treatment, respectively (Figure 5d). So, the hierarchical $ZnSnO_3/Zn_2SnO_4$ porous hollow octahedrons could be applied in the simultaneous removal of antibiotic and heavy metal pollutants from contaminated water for environmental protection.

## 4. Conclusions

To summarize, hierarchical $ZnSnO_3/Zn_2SnO_4$ porous hollow octahedrons were designed by structure and composition evolution. According to IMVS/IMPS, reflectance spectra, IPCE and Mott-Schottky plots measurements, $ZnSnO_3$ nanosheets introduced on the surface of hollow $Zn_2SnO_4$ octahedrons could provide a direct pathway for electron transport, act as light-scattering centers to improve light harvesting, and induce the flat-band potential to shift negatively. As a result, as-prepared $ZnSnO_3/Zn_2SnO_4$ hollow octahedrons could enhance the overall photovoltaic conversion efficiency by 73.1% compared to that of the $Zn_2SnO_4$ solid octahedrons. Meanwhile, the composite also exhibited

higher removal activity of Cr(VI) and CIP in single and co-existing systems under simulated sunlight irradiation. In addition, the composite photocatalyst showed good durability and stability in a co-existing system, suggesting its potential practical applications in the simultaneous removal of heavy metal and antibiotic pollutants from contaminated water.

**Supplementary Materials:** The following supporting information can be downloaded at: https://www.mdpi.com/article/10.3390/nano12122124/s1, Figure S1: Schematic of the dye-sensitized solar cell; Figure S2: SEM images of (a) $S_1$, (b) $S_2$, (d) $S_3$ and (f) $ZnSnO_3$ nanosheets; TEM images of (c) $S_2$ and (e) $S_3$. Inset: the scale bar is 50 nm in (d); Figure S3: XRD patterns of (a) $S_1$, (b) $S_2$ and (c) $S_3$; Figure S4: $N_2$ adsorption/desorption isotherms: (a) $S_2$ and (b) $S_3$; the inset is corresponding pore size distribution curves; Figure S5: Schematic illustration of light reflections and refractions in $S_2$; Figure S6: $ZnSnO_3$ nanosheets: (a) UV-vis absorption spectra; (b) Mott-Schottky plots; Inset of (a): the corresponding Tauc's curves; Figure S7: The estimated current density by integrating the IPCE spectrum; Figure S8: Controlling experiments using different radical scavengers for the removal of CIP and Cr(VI); Table S1. The calculated results of the samples about band gap energy ($E_g$), flat band potential ($E_{fb}$), $E_{CB}$ and $E_{VB}$; Table S2: Detailed photovoltaic parameters of solid $Zn_2SnO_4$-based DSSCs with film thicknesses of 10 μm and various dye-loading times; Table S3: Detailed photovoltaic parameters of DSSCs based on the $Zn_2SnO_4$ photoanode with different film thicknesses; Table S4: Detailed photovoltaic parameters of $ZnSnO_3/Zn_2SnO_4$-based DSSCs with film thicknesses of 12 μm and various dye-loading times; Table S5: Comparison of the photovoltaic performance of $ZnSnO_3/Zn_2SnO_4$ hollow octahedrons against previously reported DSSCs; Table S6: The fitting results about photocatalytic removal of the pollutants over the different samples.

**Author Contributions:** Z.L. designed the experiments and wrote the paper; K.L. carried out the synthetic experiment and measured the electrochemical performance of the samples; R.S. and C.Y. carried out the photovoltaic photocatalytic performance of the samples; X.L. analyzed the data. All authors have read and agreed to the published version of the manuscript.

**Data Availability Statement:** The data supporting the findings of this study are available by reasonable request to nylzd@nynu.edu.cn.

**Conflicts of Interest:** The authors declare no conflict of interest.

# References

1. Hussain, I.; Sahoo, S.; Mohapatra, D.; Ahmad, M.; Iqbal, S.; Javed, M.S.; Gu, S.; Qin, N.; Lamiel, C.; Zhang, K. Recent progress in trimetallic/ternary-metal oxides nanostructures: Misinterpretation/misconception of electrochemical data and devices. *Appl. Mater. Today* **2022**, *26*, 101297. [CrossRef]
2. Liu, L.; Li, M.; Chu, L.; Jiang, B.; Lin, R.; Zhu, X.; Cao, G. Layered ternary metal oxides: Performance degradation mechanisms as cathodes, and design strategies for high-performance batteries. *Prog. Mater. Sci.* **2020**, *111*, 100655. [CrossRef]
3. He, H.; Liao, A.; Guo, W.; Luo, W.; Zhou, Y.; Zou, Z. State-of-the-art progress in the use of ternary metal oxides as photoelectrode materials for water splitting and organic synthesis. *Nano Today* **2019**, *28*, 100763. [CrossRef]
4. Dou, J.; Li, X.; Li, Y.; Chen, Y.; Wei, M. Fabrication of $Zn_2SnO_4$ microspheres with controllable shell numbers for highly efficient dye-sensitized solar cells. *Sol. Energy* **2019**, *181*, 424–429. [CrossRef]
5. Hirano, T.; Takemoto, M. Photovoltaic properties of dye sensitized solar cells employing amorphous $ZnSnO_3$ as semiconducting porous film material. *Trans. Mat. Res. Soc. Jpn.* **2016**, *41*, 93–96. [CrossRef]
6. Yu, S.; Jia, X.; Yang, J.; Wang, S.; Li, Y.; Song, H. Highly sensitive and low detection limit of ethanol gas sensor based on $CeO_2$ nanodot-decorated $ZnSnO_3$ hollow microspheres. *Ceram. Int.* **2022**, *48*, 14865–14875. [CrossRef]
7. Dong, S.; Jin, X.; Wei, J.; Wu, H. Electrospun $ZnSnO_3/ZnO$ composite nanofibers and its ethanol-sensitive properties. *Metals* **2022**, *12*, 196. [CrossRef]
8. Song, J.; Lu, X.; Tian, Q.; Cui, L.; Chen, J.; Sui, Z. Dual-stable engineering enables high-performance $Zn_2SnO_4$-based lithium-ion battery anode. *J. Alloy. Compd.* **2022**, *910*, 164924. [CrossRef]
9. Tan, H.; Cho, H.; Wu, J. Binder-free $ZnO@ZnSnO_3$ quantum dots core-shell nanorod array anodes for lithium-ion batteries. *J. Power Sources* **2018**, *388*, 11–18. [CrossRef]

10. Jia, T.; An, J.; Yu, D.; Li, J.; Fu, F.; Wang, K.; Wang, W. Continuously improved photocatalytic performance of $Zn_2SnO_4/SnO_2/Cu_2O$ composites by structural modulation and band alignment modification. *Nanomaterials* **2019**, *9*, 1390. [CrossRef]

11. Anucha, C.B.; Altin, I.; Bacaksiz, E.; Stathopoulos, V.N.; Polat, I.; Yasar, A.; Yüksel, Ö.F. Silver doped zinc stannate (Ag-$ZnSnO_3$) for the photocatalytic degradation of caffeine under UV irradiation. *Water* **2021**, *13*, 1290. [CrossRef]

12. Li, Z.; Xiong, Y.; Bi, D.; Liu, Q.; Yang, C.; Zhang, J. Continuously improved gas-sensing performance of $Zn_2SnO_4$ porous octahedrons by structure evolution and further $ZnSnO_3$ nanosheets decoration. *J. Alloy. Compd.* **2022**, *901*, 163744. [CrossRef]

13. Du, L.; Zhang, H.; Zhu, M.; Zhang, M. Construction of flower-like $ZnSnO_3/Zn_2SnO_4$ hybrids for enhanced phenylamine sensing performance. *Inorg. Chem. Front.* **2019**, *6*, 2311–2317. [CrossRef]

14. Habibi, M.H.; Mardani, M. Synthesis and characterization of bi-component $ZnSnO_3/Zn_2SnO_4$ (perovskite/spinel) nano-composites for photocatalytic degradation of Intracron Blue: Structural, opto-electronic and morphology study. *J. Mol. Liq.* **2017**, *238*, 397–401. [CrossRef]

15. Manikandan, M.; Mukilraj, T.; Venkateswaran, C.; Moorthy, B.S. Exploration of photoanode characteristics of a mixed ferroelectric $ZnSnO_3$ and semiconducting $Zn_2SnO_4$ phase for photovoltaic applications. *J. Mater. Sci. Mater. Electron.* **2018**, *29*, 15106–15111. [CrossRef]

16. Wu, W.; Feng, H.; Chen, H.; Kuang, D.; Su, C. Recent advances in hierarchical three-dimensional titanium dioxide nanotree arrays for high-performance solar cells. *J. Mater. Chem. A* **2017**, *5*, 12699–12717. [CrossRef]

17. Li, Z.; Zhou, Y.; Mao, W.; Zou, Z. Nanowire-based hierarchical tin oxide/zinc stannate hollow microspheres: Enhanced solar energy utilization efficiency for dye-sensitized solar cells and photocatalytic degradation of dyes. *J. Power Sources* **2015**, *274*, 575–581. [CrossRef]

18. Jafri, N.N.M.; Jaafar, J.; Aziz, F.; Salleh, W.N.W.; Yusof, N.; Othman, M.H.D.; Rahman, M.A.; Ismail, A.F.; Rahman, R.A.; Khongnakorn, W. Development of free-standing titanium dioxide hollow nanofibers photocatalyst with enhanced recyclability. *Membranes* **2022**, *12*, 342. [CrossRef]

19. Lee, K.-H.; Han, S.-H.; Chuquer, A.; Yang, H.-Y.; Kim, J.; Pham, X.-H.; Yun, W.-J.; Jun, B.-H.; Rho, W.-Y. Effect of Au nanoparticles and scattering layer in dye-sensitized solar cells based on freestanding $TiO_2$ nanotube arrays. *Nanomaterials* **2021**, *11*, 328. [CrossRef]

20. Wang, Y.; Ma, C.; Wang, C.; Cheng, P.; Xu, L.; Lv, L.; Zhang, H. Design of $SnO_2$@Air@$TiO_2$ hierarchical urchin-like double-hollow nanospheres for high performance dye-sensitized solar cells. *Sol. Energy* **2019**, *189*, 412–420. [CrossRef]

21. Sun, X.; Yan, X.; Su, H.; Sun, L.; Zhao, L.; Shi, J.; Wang, Z.; Niu, J.; Qian, H.; Duan, E. Non-Stacked $\gamma$-$Fe_2O_3$/C@$TiO_2$ double-layer hollow nanoparticles for enhanced photocatalytic applications under visible light. *Nanomaterials* **2022**, *12*, 201. [CrossRef] [PubMed]

22. Jo, M.S.; Cho, J.S.; Wang, X.L.; Jin, E.M.; Jeong, S.M.; Kang, D.W. Improving of the photovoltaic characteristics of dye-sensitized solar cells using a photoelectrode with electrospun porous $TiO_2$ nanofibers. *Nanomaterials* **2019**, *9*, 95. [CrossRef] [PubMed]

23. Du, Y.; Niu, X.; Li, W.; An, J.; Liu, Y.; Chen, Y.; Wang, P.; Yang, X.; Feng, Q. Microwave-assisted synthesis of high-energy faceted $TiO_2$ nanocrystals derived from exfoliated porous metatitanic acid nanosheets with improved photocatalytic and photovoltaic performance. *Materials* **2019**, *12*, 3614. [CrossRef] [PubMed]

24. Saeed, M.A.; Kang, H.C.; Yoo, K.; Asiam, F.K.; Lee, J.-J.; Shim, J.W. Cosensitization of metal-based dyes for high-performance dye-sensitized photovoltaics under ambient lighting conditions. *Dye. Pigment.* **2021**, *194*, 109624. [CrossRef]

25. Dong, S.; Cui, L.; Zhang, W.; Xia, L.; Zhou, S.; Russell, C.K.; Fan, M.; Feng, J.; Sun, J. Double-shelled $ZnSnO_3$ hollow cubes for efficient photocatalytic degradation of antibiotic wastewater. *Chem. Eng. J.* **2020**, *384*, 123279. [CrossRef]

26. Peng, J.; Lin, H.; Lee, C.; Tseng, C.; Suryanarayanan, V.; Vittal, R.; Ho, K. Hierarchically assembled microspheres consisting of nanosheets of highly exposed (001)-facets $TiO_2$ for dye-sensitized solar cells. *RSC Adv.* **2016**, *6*, 14178–14191. [CrossRef]

27. Tan, B.; Toman, E.; Li, Y.; Wu, Y. Zinc stannate ($Zn_2SnO_4$) dye-sensitized solar cells. *J. Am. Chem. Soc.* **2007**, *129*, 4162–4163. [CrossRef]

28. Zhang, Q.; Dandeneau, C.S.; Zhou, X.; Cao, G. ZnO Nanostructures for Dye-Sensitized Solar Cells. *Adv. Mater.* **2009**, *21*, 4087–4108. [CrossRef]

29. Sengupta, D.; Das, P.; Mondal, B.; Mukherjee, K. Effects of doping, morphology and film-thickness of photo-anode materials for dye sensitized solar cell application—A review. *Renew. Sust. Energ. Rev.* **2016**, *60*, 356–376. [CrossRef]

30. Li, L.B.; Wang, Y.F.; Rao, H.S.; Wu, W.Q.; Li, K.N.; Su, C.Y.; Kuang, D.B. Hierarchical macroporous $Zn_2SnO_4$-ZnO nanorod composite photoelectrodes for efficient CdS/CdSe quantum dot co-sensitized solar cells. *ACS Appl. Mater. Interfaces* **2013**, *5*, 11865–11871. [CrossRef]

31. Jafarzadeh, M.; Sipaut, S.C.; Dayou, J.; Mansa, F.R. Recent progresses in solar cells: Insight into hollow micro/nano–structures. *Renew. Sust. Energ. Rev.* **2016**, *64*, 543–568. [CrossRef]

32. Wei, X.; He, X.; Wu, P.; Gong, F.; Wang, D.; Wang, S.; Lu, S.; Zhang, J.; Xiang, S.; Kai, T.; et al. Recent advances in the design of semiconductor hollow microspheres for enhanced photocatalytic water splitting. *Int. J. Hydrogen Energ.* **2021**, *46*, 27974–27996. [CrossRef]

33. Yashwantrao, G.; Saha, S. Perspective on the rational design strategies of quinoxaline derived organic sensitizers for dye-sensitized solar cells (DSSC). *Dye. Pigment.* **2022**, *199*, 110093. [CrossRef]

34. Law, M.; Greene, L.E.; Johnson, J.C.; Saykally, R.; Yang, P.D. Nanowire dye-sensitized solar cells. *Nat. Mater.* **2005**, *4*, 455–459. [CrossRef]

35.  Sasidharan, S.; Jagadeesh, A.; Pradhan, S.C.; Nair, B.N.; Mohamed, A.A.; Unni, K.N.N.; Soman, S.; Hareesh, U.N. ZnO hierarchical structures as sacrificial inclusions for enhanced performance under full sun and indoor light in bifacial dye sensitized solar cells. *Sol. Energy* **2021**, *226*, 214–224. [CrossRef]

36.  Merazga, A.; Al-Zahrani, J.; Al-Baradi, A.; Omer, B.; Badawi, A.; Al-Omairy, S. Optical band-gap of reduced graphene oxide/$TiO_2$ composite and performance of associated dye-sensitized solar cells. *Mat. Sci. Eng. B* **2020**, *259*, 114581. [CrossRef]

37.  Akman, E.; Akin, S.; Ozturk, T.; Gulveren, B.; Sonmezoglu, S. Europium and terbium lanthanide ions co-doping in $TiO_2$ photoanode to synchronously improve light-harvesting and open-circuit voltage for high-efficiency dye-sensitized solar cells. *Sol. Energy* **2020**, *202*, 227–237. [CrossRef]

38.  Khan, M.W.; Zuo, X.; Yang, Q.; Tang, H.; Rehman, K.M.U.; Wu, M.; Li, G. Functionalized multi-walled carbon nanotubes embedded with nanoflakes boost the short-circuit current of Ru(II) based dye-sensitized solar cells. *Dye. Pigment.* **2020**, *181*, 108573. [CrossRef]

39.  Devadiga, D.; Selvakumar, M.; Shetty, P.; Santosh, M.S. Recent progress in dye sensitized solar cell materials and photo-supercapacitors: A review. *J. Power Sources* **2021**, *493*, 229698. [CrossRef]

40.  Agrawal, A.; Siddiqui, S.A.; Soni, A.; Sharma, G.D. Advancements, frontiers and analysis of metal oxide semiconductor, dye, electrolyte and counter electrode of dye sensitized solar cell. *Sol. Energy* **2022**, *233*, 378–407. [CrossRef]

41.  Dou, J.; Lia, Y.; Wu, J.; Chang, Y.J.; Wei, M. Improving the photovoltaic performance of $Zn_2SnO_4$ solar cells by doping $Sr^{2+}$/$Ba^{2+}$ ions: Efficient electron injection and transfer. *Sol. Energy* **2018**, *165*, 122–130. [CrossRef]

42.  Ursu, D.; Banică, R.; Vajda, M.; Baneasa, C.B.; Miclau, M. Investigation of silver nanowires in $Zn_2SnO_4$ spheres for enhanced dye-sensitized solar cells performance. *J. Alloy. Compd.* **2022**, *902*, 163890. [CrossRef]

43.  Li, B.; Guo, E.; Wang, C.; Yin, L. Novel Au inlaid $Zn_2SnO_4$/$SnO_2$ hollow rounded cubes for dye-sensitized solar cells with enhanced photoelectric conversion performance. *J. Mater. Chem. A* **2016**, *4*, 466–477. [CrossRef]

44.  Karimi, V.; Asemi, M.; Ghanaatshoar, M. Improving photovoltaic properties of ZTO-based DSSCs using surface modifcation of $Zn_2SnO_4$ nanoparticles prepared by co-precipitation method. *Mat. Sci. Semicon. Proc.* **2021**, *127*, 105664. [CrossRef]

45.  Siwatcha, S.; Kundua, V.S.; Kumarb, A.; Kumara, S.; Chauhana, N.; Kumaria, M. Effect of novel ZnO/$Zn_2SnO_4$ photoanode on the performance of dye sensitized solar cell. *Optik* **2019**, *194*, 163117. [CrossRef]

46.  Saeed, M.A.; Yoo, K.; Kang, H.C.; Shim, J.W.; Lee, J.-J. Recent developments in dye-sensitized photovoltaic cells under ambient illumination. *Dye. Pigment.* **2021**, *194*, 109626. [CrossRef]

47.  Lei, D.; Xue, J.; Bi, Q.; Tang, C.; Zhang, L. 3D/2D direct Z-scheme photocatalyst $Zn_2SnO_4$/CdS for simultaneous removal of Cr(VI) and organic pollutant. *Appl. Surf. Sci.* **2020**, *517*, 146030. [CrossRef]

48.  Li, S.; Chen, J.; Hu, S.; Jiang, W.; Liu, Y.; Liu, J. A novel 3D Z-scheme heterojunction photocatalyst: $Ag_6Si_2O_7$ anchored on flower-like $Bi_2WO_6$ and its excellent photocatalytic performance for the degradation of toxic pharmaceutical antibiotics. *Inorg. Chem. Front.* **2020**, *7*, 529–541. [CrossRef]

49.  Li, Z.; Bi, D.; Zhao, Y.; Liu, R.; Ye, J.; Zhou, Y. In situ growth of zinc oxide nanoribbons within the interstices of a zinc stannate nanoplates network on compacted woven metal wires and their enhanced solar energy application. *Electrochim. Acta* **2018**, *262*, 124–134. [CrossRef]